Applications in Energy and Combustion Science 27 (2026) 100524

Contents lists available at ScienceDirect

Applications in Energy and Combustion Science

journal homepage: www.elsevier.com/locate/jaecs

Flame lift-off dynamics in a thermoacoustically self-excited swirl flame: A sensitivity analysis based on LES

Michael Pries *, Andreas Fiolitakis

German Aerospace Center (DLR), Institute of Combustion Technology, Pfaffenwaldring 38-40, 70569 Stuttgart, Baden-Württemberg, Germany

ARTICLE INFO

Keywords:
Compressible LES
Self-excited thermoacoustic instability
Partially-premixed combustion
Gas turbine combustion
PRECCINSTA
Turbomeca

ABSTRACT

In this work, compressible Large-Eddy Simulations are used to investigate a well-established swirl flame. This swirl flame is known for its strong self-excited thermoacoustic oscillations. Due to the availability of an extensive experimental database, the flame is frequently studied numerically, although a limited agreement is observed between experimental and numerical data. It is found that this limited agreement can be attributed to the investigated operational point which is close to an unstable region where the flame switches between attached and lifted state. This results in a configuration that is highly sensitive to small differences between the numerical and experimental boundary conditions. Targeted investigations are used to demonstrate that parameters such as the amplitude of the pressure oscillation as well as minor deviations in the operational point significantly influence the computational results. Taking these details into account, a very good agreement with experimental data is achieved. Subsequently, it is demonstrated that the processes inside the swirler, where fuel and oxidizer mix, are highly unsteady and must be modeled with caution. Moreover, coherent flow structures are found to be present during sporadic events of flame lift-off. Although this behavior is reported in literature at other operational points, this is shown for the first time for the operational point considered here.

1. Introduction

Thermoacoustic instabilities remain a major risk in the design and development of modern gas turbines. To mitigate this risk, model-based approaches describing the phenomenon are essential. However, for such model-based approaches, the major challenge is that the computation of this type of instabilities is non-trivial and still an active research area. In literature, different modeling techniques exist to capture the complex feedback loop between heat release and acoustics. A rigorous approach is to solve such problems by means of compressible Large-Eddy Simulations (LES). This has the advantage that a solution to both the flow field as well as the acoustics is obtained simultaneously. The data from such compressible LES are extensive and can provide means to get deep insight into relevant physical phenomena. However, compressible LES are computationally expensive and require rigorous validation. For this reason, studies often focus on model combustors. Nevertheless, these model combustors are also relevant for the development of modern gas turbines, as they include key features such as swirling flows. One such model burner is the PRECCINSTA (also known as Turbomeca) combustion device [1–3]. This burner features a swirl stabilized flame that is operated under lean conditions at atmospheric pressure. Depending on the operational point, a strong self-excited thermoacoustic instability is observed. Such an operational point is obtained for an equivalence ratio of $\phi = 0.7$ at a thermal power of $P_{\mathrm{th}} = 25\,\mathrm{kW}$ where the burner is operated at technically premixed conditions with methane as fuel and air as oxidizer. Here, technical premixing refers to a separate injection of fuel and oxidizer upstream the combustion chamber inside the swirler. The most comprehensive experimental study for this operational point is given in [3] and comprises velocity, species, temperature and OH*-chemiluminescence measurements with the intent of providing the data for validation of numerical methods. Numerous experimental studies followed upon the early studies of [3]. Examples are the investigations concerning the occurrence of coherent structures of the swirl stabilized flame demonstrated by [4,5] or the switching between attached and lifted flame by [6–9]. More recently, the work of [10,11] display the influence of hydrogen addition onto the thermoacoustic behavior of this swirled flame. In these studies, different operational points of the burner are investigated, covering both technical premixing and perfectly premixed conditions. However, the initial work of [3] remains the most exhaustive data set for a thermoacoustically self-excited operational point. For this reason, the aforementioned operational point is often studied by means of compressible LES to either test new approaches or to further the understanding of the emerging thermoacoustic phenomena [12–21]. In these studies, the computational

* Corresponding author.
E-mail address: michael.pries@dlr.de (M. Pries).

https://doi.org/10.1016/j.jaecs.2026.100524
Received 13 February 2026; Received in revised form 12 May 2026; Accepted 5 June 2026
Available online 10 June 2026

results differ strongly concerning the dominant thermoacoustic mode frequency as well as the corresponding lift-off height of the flame above the burner. For some studies such as [12,13,19,20] the flame position based on the burner exit temperatures agrees well with the experiments of [3], but the frequency of the thermoacoustic instability is not matched. Others obtain a very good agreement of the dominant mode frequency [14,16,21] but fail to match the temperatures above the burner indicating a poor agreement of the flame position. To our knowledge, the studies of [15,17] show the best agreement for both, frequency and flame lift-off height, yet.

In the present work, we contemplate that these disagreements can not only be attributed to a lack in numerical model fidelity but could also be related to the thermoacoustic operational point chosen by [3] which resides close to an unstable region. The proximity to such an unstable region further results in a highly sensitive operational point where small deviations in setup (e.g. mass-flow rates and acoustic velocities) lead to major differences in flame behavior. This adds to the complexity of the chosen operational point and contributes to the fact, that despite numerous attempts this case has not yet been calculated numerically with sufficient accuracy.

In the present context, an unstable region is characterized by a random switching between lifted and attached flame during the operation of the combustion device. Such behavior is already reported in [4–8] at different operational points for the investigated device. Concerning the operational point of [3], the studies of [21,22] already show clear discrepancies when even minor deviations in the experimental setup are present. Based on the averaged OH*-Chemiluminescence data reported in [21], a lifted flame is observed, whereas an attached flame is found in [3]. Concerning the work of [22], again discrepancies with [3] are apparent. Here, under slightly richer conditions and a small decrease in thermal power, an unstable flame is found switching with approximately 10 Hz between attached and lifted state. Based on these observations from literature, it can already be concluded that the operational point considered resides close to an unstable region.

The present work demonstrates that the difficulties observed in the literature regarding the satisfactory modeling of the burner are directly related to the fact that the selected operational point is close to a region where unstable flame behavior occurs. This manifests itself in an extremely high sensitivity of the numerical solution to model parameters that directly influence the flame behavior. To illustrate this, three different aspects of the numerical model are investigated in detail, namely (1) the acoustic velocity at the flame root, (2) the equivalence ratio in vicinity of the flame, and (3) the technical mixing of air and fuel. Regarding the first aspect, the acoustic velocities at the flame root are systematically modified by varying the transmissivity of sound waves at the outflow boundary. It is shown in Section 4.2, that a low transmissivity favors blow-off of the flame at the present operating conditions and affects strongly the numerical solution close to the burner exit. Likewise, for the second aspect, the effects of slightly more fuel-rich conditions in the flame zone is investigated in Section 4.3 through modifying the fuel and air mass-flow rates in the computation. To address the third aspect, the general assumption of a good, albeit not perfect, mixing for the reactant stream at the entrance to the combustion chamber is challenged in Section 4.5 (cf. [1–3,23]) through an investigation of the highly unsteady processes inside the swirler. Incorporating the findings of these three investigations into the numerical simulation, the operational point is studied in more detail in Section 4.6 with a particular emphasis on the dynamics that lead to sporadic flame lift-off at these unstable conditions. Such lift-off events for the operational point investigated have so far not been observed numerically. The presented results therefore advance the understanding of the considered well-established model combustor and are also relevant for other technical devices where flame anchoring might be critically influenced through acoustic effects.

2. The PRECCINSTA model burner

The schematics of the PRECCINSTA combustion device is given in Fig. 1. Here a cut through the x_1–x_3 plane at $x_2 = 0$ mm is shown. As indicated, the origin of the coordinate system is placed at the tip of the central body. The combustor consists of several sections. Air is entering the system at the most upstream point and is channeled into the air plenum. From there, the air is guided into the swirler where it is mixed with the fuel coming from the fuel plenum. The swirler has a total of twelve vanes where each vane is equipped with an individual fuel port of 1 mm diameter. In this way the fuel is injected with a high momentum into the air stream. Generally, a good mixing of air and fuel streams is assumed for this kind of configuration. The now technically premixed, swirled mixture is then channeled into the combustion chamber via a connecting duct. Inside this duct, the central body is placed concentrically. At the exit plane of the duct, the cylindrical cross-section transitions into a square with a lateral length of 85 mm. The combustion chamber has a total length of 114 mm and all four side walls are equipped with quartz glass windows each with a thickness of 1.7 mm. These quartz glass sheets are held in place by four metal corner posts. At the downstream location of the combustion chamber, the cross section transitions back to a cylindrical shape, and the exhaust gases leave the device through the converging outlet section.

3. Numerical method and modeling approach

In the following sections relevant modeling details and assumptions are stated. Starting with a definition of the set of equations needed to solve a compressible reactive system, the section is concluded with an overview of the numerical solution strategy and the numerical setup applied for the considered computational studies.

3.1. Filtered transport equations

The spatially Favre-filtered balance equations for mass, momentum, energy, and the transport equations for species mass fractions are given by (Einstein notation)

$$\frac{\partial \overline{\rho}}{\partial t} + \frac{\partial \overline{\rho}\widetilde{u}_i}{\partial x_i} = 0, \tag{1}$$

$$\frac{\partial \overline{\rho}\widetilde{u}_i}{\partial t} + \frac{\partial \overline{\rho}\widetilde{u}_i\widetilde{u}_j}{\partial x_j} - \frac{\partial \overline{\tau}_{ij} + \tau_{t,ij}}{\partial x_j} + \frac{\partial \overline{p}}{\partial x_i} = 0, \tag{2}$$

$$\frac{\partial \overline{\rho}\widetilde{E}}{\partial t} + \frac{\partial \overline{\rho}\widetilde{u}_i\widetilde{E}}{\partial x_i} + \frac{\partial \widetilde{u}_i\overline{p}}{\partial x_i} - \frac{\partial \widetilde{u}_j\left(\overline{\tau}_{ij} + \tau_{t,ij}\right)}{\partial x_i} + \frac{\partial \overline{q_i} + q_{t,i}}{\partial x_i} = 0, \tag{3}$$

and

$$\frac{\partial \overline{\rho}\widetilde{Y}_\alpha}{\partial t} + \frac{\partial \overline{\rho}\widetilde{u}_i\widetilde{Y}_\alpha}{\partial x_i} + \frac{\partial \overline{j}_{\alpha i} + j_{t,\alpha i}}{\partial x_i} = \overline{S}_\alpha. \tag{4}$$

In Eqs. (1)–(4), x_i are the spatial coordinates, t the physical time, ρ the density, u_i is the velocity vector, p the pressure, E is the specific total energy, and Y_α the mass fraction for the species α. The viscous stress tensor is defined through

$$\overline{\tau}_{ij} = 2\mu\left(\widetilde{S}_{ij} - \delta_{ij}\frac{1}{3}\widetilde{S}_{kk}\right), \tag{5}$$

with

$$\widetilde{S}_{ij} = \frac{1}{2}\left(\frac{\partial \widetilde{u}_i}{\partial x_j} + \frac{\partial \widetilde{u}_j}{\partial x_i}\right), \tag{6}$$

where μ is the dynamic viscosity. The vector of the heat flux is given by

$$\overline{q}_i = -\lambda\frac{\partial \widetilde{T}}{\partial x_i} + \sum_{\alpha=1}^{N_s}\widetilde{h}_\alpha j_{\alpha i}, \tag{7}$$

and the diffusive mass flux is

$$\overline{j}_{\alpha i} = -\overline{\rho}D_\alpha\frac{\partial \widetilde{Y}_\alpha}{\partial x_i}. \tag{8}$$

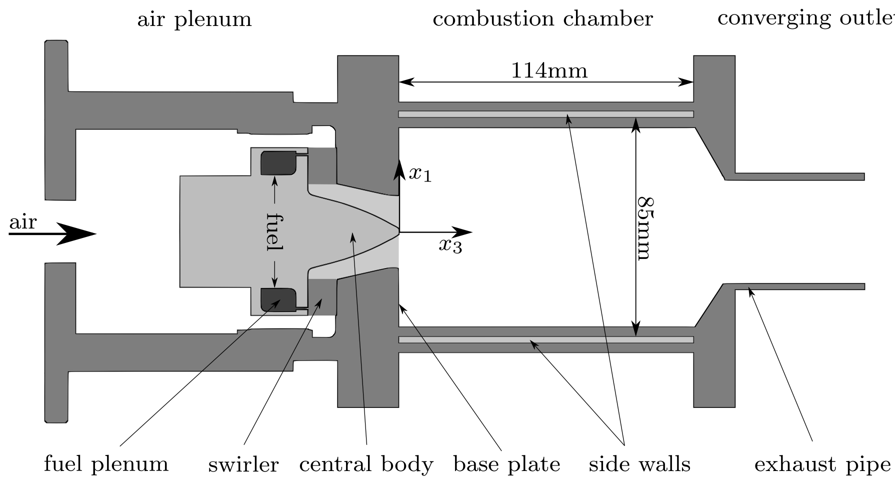

Fig. 1. Schematic drawing of the investigated combustion device [1–3].

Here, λ is the thermal conductivity, h_α the specific enthalpy of the pure substance α, and D_α the respective diffusion coefficient. The chemical source term is given by S_α whereas the specific total energy is defined as the sum of the specific internal energy and the specific kinetic energy. A mixture of thermally perfect gases is assumed where the state equation for an ideal gas applies. Filtered values are denoted by $\overline{(\cdot)}$ whereas a Favre-filtered value is denoted by $\widetilde{(\cdot)}$. Due to the filtering, the subgrid-scale stress tensor $\tau_{t,ij}$, the subgrid-scale heat flux $q_{t,i}$, and the subgrid-scale species mass flux $j_{t,\alpha i}$ arise. It is assumed that no further subgrid terms e.g. through the filtering of the ideal gas law are relevant. The models for the subgrid-scale terms are outlined in Section 3.3.

3.2. Numerical solution scheme

Eqs. (1)–(4) are solved using the Implicit Characteristic Splitting (ICS)-scheme as described in [24]. Using the ICS-scheme the set of transport and balance equations are split up into an advective and an acoustic subsystem. Both subsystems are solved independently from each other. The advective subsystem is discretized using a temporal second order implicit Crank–Nicolson scheme where a Newton–Raphson method is used to solve the non-linear system. For the acoustic subsystem a pressure correction equation is derived which is also solved in a fully implicit manner. The scheme is implemented in the in-house code ThetaCOM [25,26] using a cell-vertex [27] approach where based on a primary grid a median-dual mesh is constructed. A detailed description of the method is given in [24].

3.3. Closure models for subgrid-scale fluxes

The subgrid-scale stress term $\tau_{t,ij}$ is closed under the eddy-viscosity assumption modeling it as

$$\tau_{t,ij} = \underbrace{2\mu_t\left(\widetilde{S}_{ij} - \frac{1}{3}\delta_{ij}\widetilde{S}_{kk}\right)}_{\text{deviatoric}} + \underbrace{\frac{2}{3}\mu_t\delta_{ij}\widetilde{S}_{kk}}_{\text{isotropic}}. \tag{9}$$

According to [28], the isotropic term is assumed to be small and is for this reason neglected. Here, the eddy viscosity μ_t is modeled according to the wall adapting local eddy viscosity (WALE) model of [29]. In this model a case dependent constant needs to be defined for which the value 0.1 is used. The subgrid-scale heat flux is modeled using a gradient diffusion approach given by

$$q_{t,i} = -\lambda_t \frac{\partial \widetilde{T}}{\partial x_j} + \sum_{\alpha=1}^{Ns} \widetilde{h}_\alpha j_{t,\alpha i}. \tag{10}$$

Here, λ_t is the turbulent heat conductivity coefficient calculated using the eddy-viscosity together with the turbulent Prandtl number Pr_t and the isobaric heat capacity c_p through

$$\lambda_t = \frac{\mu_t c_p}{Pr_t}. \tag{11}$$

A similar approach is chosen for the subgrid-scale species diffusion defined by

$$j_{t,\alpha i} = -\overline{\rho} D_t \frac{\partial \widetilde{Y}_\alpha}{\partial x_i}. \tag{12}$$

The turbulent species diffusion coefficient is calculated using the eddy-viscosity and the turbulent Schmidt number Sc_t as

$$D_t = \frac{\mu_t}{\overline{\rho} Sc_t}. \tag{13}$$

In this work, the turbulent Prandtl and Schmidt numbers are set to $Pr_t = Sc_t = 0.4$ for all reactive simulations.

3.4. Combustion modeling

For the thermoacoustically unstable operational point, the PRECCINSTA combustor is periodically switching between states of partial extinction and reignition. This behavior requires a combustion model that is able to capture these processes. For this reason, a finite-rate chemistry approach is chosen. The chemical kinetics are described using a reduced variant of the DLR-Concise (DC1S29) mechanism given in [30]. To close the filtered chemical source term $\overline{S}_\alpha$, an assumed probability function approach is used. Details concerning this approach are found in [31].

3.5. Spatial and temporal discretization

A hybrid meshing approach is chosen for the spatial discretization of the combustor. In total, three different meshes are considered which are similar in topology but differ in the total amount of control volumes. An overview of the number of points and the number of cells in the primary grid for the three meshes is given in Table 1. As shown in Table 1, mesh one is the coarsest, containing the fewest mesh points, while mesh three is the finest with the highest number of points among the considered meshes. According to [12] it may be important to include the fuel plenum to match the dominant pressure mode. However, the results of [32] show that a good agreement can also be achieved without the explicit modeling of the fuel plenum. Nevertheless, the fuel plenum is included in the present study. This moves the fuel inflow boundary away from the swirler vane injection holes, thereby allowing the capture of their acoustic characteristics. The grid topology is adjusted

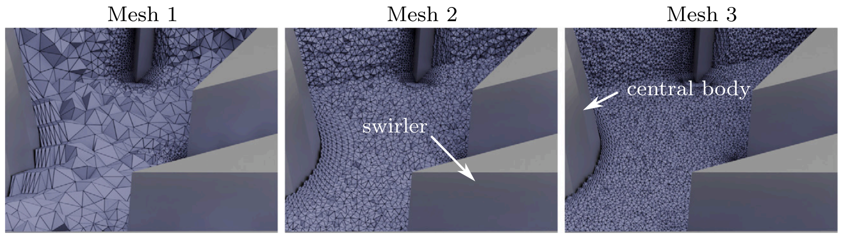

Fig. 2. Cut through the swirler region. Displayed are meshes one to three.

Table 1
Number of points and number of cells in the primary grid for the meshes one to three.

Mesh	No. of points	No. of cells
1	4.6M	11.8M
2	11.9M	32.2M
3	24.1M	91.6M

to cluster a large number of cells in regions where highly dynamic processes such as mixing and combustion occur. For this reason, the smallest cells are found inside the swirler region and at the entrance to the combustion chamber. In this area, the shortest cell length scales of the tetrahedrals range from 0.5 mm for mesh one to 0.1 mm for mesh three. As an example, this is shown for the swirler region in Fig. 2, where a cut through the meshes one to three is given. Prism layers are placed at all solid walls to obtain a sufficient wall resolution. This is also shown in Fig. 2. The computational time step throughout the conducted simulations varies between 0.05 μs and 0.10 μs. This results in a maximal convective Courant–Friedrichs–Lewy (CFL) number in the range of 0.23 to 0.84.

3.6. Boundary conditions

To allow acoustic disturbances to leave the computational domain at the outflow boundary, the Navier–Stokes Characteristic Boundary (NSCBC) method proposed by [33] is employed in this work. A detailed description of the approach in combination with the ICS-scheme is given in [24]. In [34] it is shown that the outflow modeling significantly influences both the thermoacoustic mode frequency and flame dynamics. For this reason, the effect of the outflow boundary is investigated here systematically. To this end, two different computational runs are defined, namely cases one and two (cf. Table 2). For both cases, the outflow boundary is partially reflective, i.e. the characteristic wave associated with the amplitude variation L_1 is modeled according to [35] by

$$L_1 = \sigma \left(1 - M_{\mathrm{out}}^2\right) \frac{\overline{c}}{L_{\mathrm{out}}} \left(\overline{p} - p_\infty\right). \tag{14}$$

In Eq. (14), $M_{\mathrm{out}} = 0.1$ is the maximal occurring Mach number at the outflow, $L_{\mathrm{out}} = 0.114\,\mathrm{m}$ the characteristic domain size, and $p_\infty = 101325\,\mathrm{Pa}$ the ambient pressure. σ is the parameter which is used here to control the reflection of the outflow. For case one, the optimal value of $\sigma = 0.27$ [33] is used whereas $\sigma = 0.06$ is employed for case two. At the frequency of 275 Hz, which is the base frequency of the pressure oscillations observed in this burner, this decrease in σ reduces the magnitude of the reflection coefficient by a factor of four. Consequently, higher acoustic losses are obtained in case two. Concerning the inflow boundaries, reflective boundary conditions are used for cases one and two. In addition to these two cases, a third case is defined in Table 2. This case three is essentially the same as case two, except that the mass-flow rates of fuel and air are slightly altered. Air is assumed to be a mixture of oxygen and nitrogen with a composition of $Y_{\mathrm{O}_2} = 0.233$ and $Y_{\mathrm{N}_2} = 0.767$. The temperature of all incoming streams is kept constant at $T_{\mathrm{in}} = 320\,\mathrm{K}$ for all cases and is chosen in accordance to the data provided in [3]. Considering the walls, constant temperature boundary conditions are assumed. For this purpose, the temperature profiles for the combustion chamber side walls as well as the base plate are taken from the measurement data provided in [6,36]. Based on the measured temperatures indicated by the symbols in Fig. 3, a polynomial fit is computed. This polynomial fit is used in the computation to express the spatial dependence of the wall temperatures for this case. The resulting temperature profiles are shown in Fig. 3 by the solid lines. It has to be noted that the measurements of [6] are carried out for a reduced thermal power under perfectly premixed conditions. The experimental results of [36] are obtained at the same thermal power for a combustor with a different swirler but with almost identical combustion chamber. However, in the experiment the temperature at the walls of the combustion chamber depends on the operational conditions and may vary with flame position. Hence, the applied thermal boundary conditions in the present computations introduce simplifications through the assumption of constant temperature walls. As demonstrated in [37,38] through conjugate heat-transfer calculations, the thermal boundary conditions can influence the occurrence of thermoacoustic instabilities as well as flame anchoring. However, all these calculations are performed at a significantly lower thermal power of 10 kW, where an accurate computation of heat losses may indeed have an essential impact on the solution. For the present operational point at a significantly higher thermal power of 25 kW, the accurate modeling of wall temperatures appears to be of less importance. For example, computational data for constant wall temperatures given in [18,39] show a very good agreement to experimental data. Only the dynamic behavior of the flame close the burner exit appears to depend on the choice of thermal boundary conditions at the central body of the swirler [39]. However, one has to consider that in [39] a considerably coarser mesh is used compared to [37,38] which is suitable for capturing time averaged heat transfer rates but not sufficiently fine to resolve the “detailed boundary layer turbulence structure accurately” [39]. Therefore, one cannot clearly attribute in [39] the difficulties of capturing flame dynamics solely to a potentially insufficient modeling of the thermal boundary condition at the central body. For these reasons, the use of data given in conditions [6,36] to model the temperature distribution is justified for the present investigation. Additionally, wall temperatures obtained from the conjugate heat-transfer calculation in [38] also justify the use of the applied temperature profile data. Further, the temperature of the central body tip is set to 520 K. Towards the swirler this value is reduced linearly until 320 K is reached. This is also the wall temperature of the remaining constant temperature walls and matches the temperatures of the technically premixed mixture at the entrance of the burner reported in [3]. Further, the quartz glass panes are mounted floating between the base plate, metal corner posts and end plate in the experiment. No sealing is introduced, hence additional damping is to be expected in the experimental data (cf. [16,21]). However, as no data is available on the damping characteristics of the quartz glasses, this is not taken into account in the present work. Instead, the combustor side walls are assumed to be acoustically fully reflective.

4. Results

First, the influence of the computational grids is investigated in Section 4.1. After the requirements for a sufficient spatial resolution

Table 2
Inflow and outflow conditions for the cases one to three.

Case	inflow		outflow
	$\dot{m}_{\mathrm{air}}$ [g/min]	$\dot{m}_{\mathrm{fuel}}$ [g/min]	σ
1	734.2	30.00	**0.27**
2	734.2	30.00	0.06
3	**723.0**	**30.45**	0.06

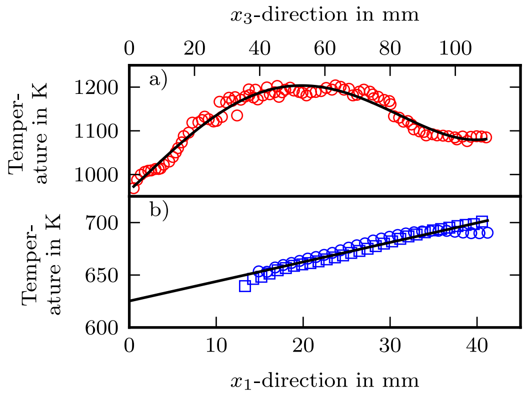

Fig. 3. Prescribed temperature profiles for the walls inside the combustion chamber. (a) temperature profile of the side walls. (b) temperature profile of the base plate. (——) polynomial fit, (○) measurement data Flame B from [36], (○) and (□) measurement data of [6].

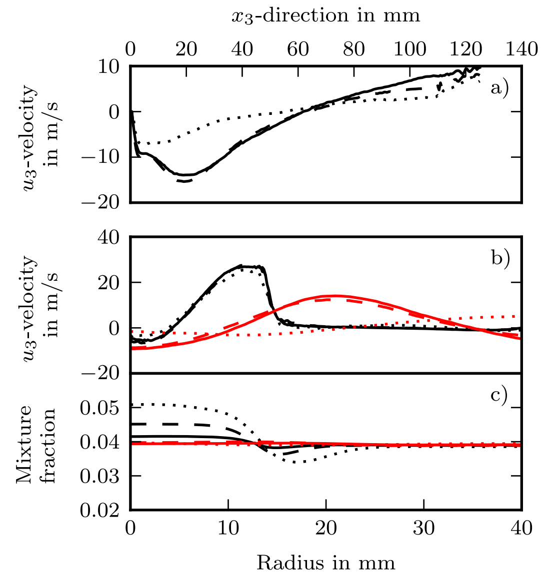

Fig. 4. Comparison of the inert simulations on meshes one to three. (a) axial velocity along centerline. (b) axial velocity along the radius at x_3 = 1.5 mm (black) and at x_3 = 35 mm (red). (c) mixture fraction along the radius at x_3 = 6 mm (black) at x_3 = 35 mm (red). (⋯⋯) mesh 1, (- - -) mesh 2, (——) mesh 3.

are obtained, the effects of the amplitude of the pressure oscillations and the acoustic velocities is investigated in Section 4.2. For this purpose cases one and two are compared. Subsequently, the effects of an enriched flame and, therefore, an increased flame speed are looked at in Section 4.3 by comparing cases two and three. Since case three shows the most promising results it is rigorously verified against available experimental data in Section 4.4. From this point on, all further investigations are based on case three. This includes a closer look at the mixing as well as the flame shapes and coherent flow structures in Sections 4.5 and 4.6.

4.1. Grid sensitivity study for inert flow

In order to obtain a sufficient spatial resolution, compressible LES are carried out. An inert flow is considered first on the meshes one to three (cf. Section 3.5). The boundary conditions are selected similar to those applied in the reactive cases as presented in Section 3.6. All three computations are started from an identical stationary incompressible solution. A comparison of the time-averaged axial velocity as well as the mixture fraction for the different meshes is given in Fig. 4. The axial velocity along the centerline inside the combustion chamber starting at the tip of the central body is shown in Fig. 4a. Comparing the axial velocities across the different meshes, it is apparent that the largest deviations are found for mesh one, which has the coarsest resolution. Especially the large recirculation zone extending approximately 60 mm into the combustion chamber is not well captured in comparison to the finer meshes. In Fig. 4b, the averaged axial velocity is displayed over the radius for two different heights above the base plate. The black lines denote profiles at x_3 = 1.5 mm whereas the profiles in red are taken at x_3 = 35 mm. In addition to time averaging, spatial averaging is performed over twelve equiangular spaced lines. It is observed that, at x_3 = 1.5 mm, the differences between the three meshes are small, whereas significant deviations are found at x_3 = 35 mm. In terms of velocity a good agreement is obtained for the meshes two and three. Concerning a transported scalar, the distributions for the averaged mixture fraction along the radius at the heights x_3 = 6 mm and x_3 = 35 mm are given in Fig. 4c. In contrast to the averaged axial velocities, deviations directly above the burner are present between the meshes two and three. Further downstream, these deviations diminish as the distribution of the mixture fraction along the radius becomes more homogeneous. In addition to the computations of inert flow, a grid study is performed also for reactive flows on meshes two and three. Here, the thermoacoustic instabilities also strongly influence the spatial distribution of the computed quantities. For this reason, Fig. 5 compares the mixture fraction and the u_3-velocity for different heights above the base plate. The results presented in Fig. 5 for mesh two and three are averaged over a single period of pressure oscillation inside the combustion chamber. A comparison of the results again reveals good agreement for the u_3-velocity. Additionally, also the mixture fraction shows reasonably good agreement between the two meshes at the investigated positions. This leads to the conclusion that mesh two provides a sufficient resolution for the reactive computation conducted herein. Therefore, mesh two is chosen for all subsequent reactive simulations, as it offers an acceptable balance between resolution and computational costs.

4.2. Influence of the outflow modeling

To assess the influence of the outflow modeling, case one and case two are compared. The lower reflection factor in case two permits for higher acoustic losses as compared to case one. This reduces the root mean square (RMS) values of pressure inside the combustion chamber from 1978 Pa for case one to 1548 Pa for case two. In Fig. 6a, the power spectral densities (PSD) of the combustion chamber pressure are plotted for the cases one and two. Alongside the computed results, the experimental pressure PSD reported in [16] is shown. The pressure PSDs are computed using Welch's method with a Hanning window function and an overlap of 50%. For the computed pressure signal, four overlapping, windowed segments are considered in the analysis. Comparing the PSDs of the computed chamber pressure, a slight increase in frequency is obtained for case two as compared to case one. Further, the maximal value at the dominant peak is slightly lower for case two. Considering the local maxima at the higher harmonics at 500 Hz and 740 Hz, the differences become more apparent and lower values are found for case two. Comparing the computed cases to the

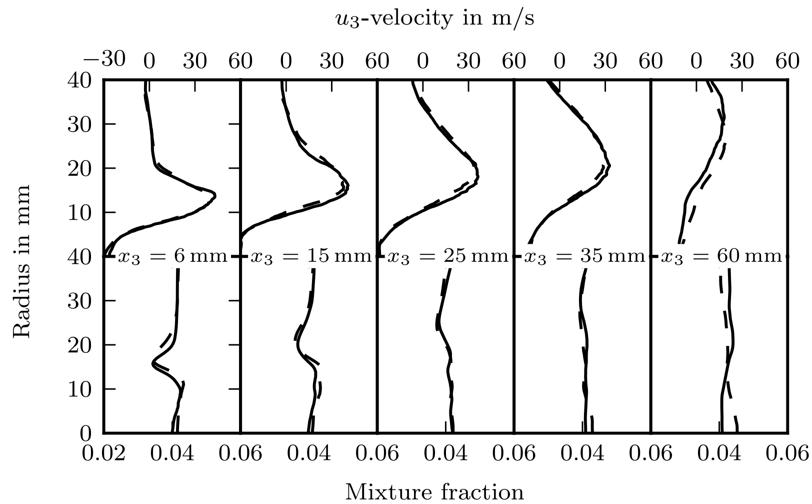

Fig. 5. Comparison of meshes two and three for the reactive case at $x_3 \in \{6, 15, 25, 35, 60\}$ mm. Results of the mixture fraction and the u_3-velocity averaged over one oscillation period of the combustion chamber pressure are shown. (- - -) mesh 2, (——) mesh 3.

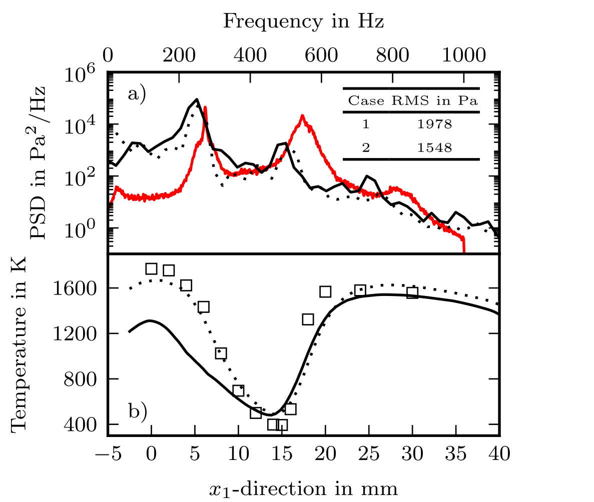

Fig. 6. Comparison of case 1 and case 2. (a) power spectral density of the pressure inside the combustion chamber. (b) temperature above the burner at $x_3 = 6$ mm. (——) case 1, (⋯⋯) case 2, (——) measurements from [16], (□) measurements from [3].

experimental results, approximately 20 Hz lower frequencies are found for the numerical results at the dominant mode. Nonetheless, the absolute values for the peak amplitude are matched well compared to the experimental findings given in [16]. Additionally, a pronounced third peak at around 740 Hz is found for case one whereas this is not seen in the experimental data nor for case two. Overall, a good agreement is found for both cases comparing the computed results with the available experimental data. However, the modification concerning the outflow in case two results in a slight improvement of the overall agreement between computed combustion chamber pressure and the experimental data. By contrast, significant differences between the cases one and two are found close to the central body as shown in Fig. 6b. Here, the Favre averaged temperatures are displayed along the x_1-axis at a height above the burner at $x_3 = 6$ mm for both cases. While case two does match the temperatures very well, the temperatures at x_1 below 10 mm are found to be too low in case one. A possible reason for the differences in the averaged temperature is a significant variation in flame behavior between cases one and two. In case one, the lower averaged temperatures may result from numerous low temperature events evoked by flame lift-off. These events then accumulate to the observed lower averaged temperatures. By contrast, fewer lift-off events might be present for case two resulting in an overall higher temperature directly above the burner. Indeed, this is confirmed by the temporal evolution of temperature above the burner, as shown in Fig. 7a. For case one, a frequent switch between low and high temperature events takes place whereas this is not observed for case two. Additionally, Figs. 7b and 7c show the instantaneous heat release in the x_1–x_3 plane at $x_2 = 0$ mm at two distinct time instances. Here it becomes clear that these low temperature events are accompanied by a temporary flame lift-off. For instance, this is observed at $t_1 = 49$ ms, where for case one a low temperature and a lifted flame is found. In return, for case two the temperature remains high and the flame is attached to the central body. However, for the second time instance at $t_1 = 74$ ms in both cases high temperature and attached flames are found. To obtain a better understanding of the differences in the transient flame behavior, a video sequence is available in the supplemental materials *Video S2*. In the video, unsteady isocontours of temperature in the x_1–x_3 plane as well as the volume rendering of the three dimensional heat release demonstrate differences in the flame characteristics. A detachment of the flame root from the central body and a subsequent flame lift-off is observed during phases of low temperature above the central body for case one only. However, flashback into the duct connecting swirler and combustion chamber occurs in both cases. The temporary lift-off events in case one are caused by higher velocity fluctuations at the entrance into the combustion chamber as compared to case two. This is shown in Fig. 8a where the area averaged velocity fluctuations in the x_1–x_2 plane at $x_3 = 0$ mm are plotted over time. Alongside the temporal data, the standard deviations are annotated. Comparing the data given in Fig. 8a, it is seen that overall, higher values are found for case one as compared to case two. In detail, the modifications to the outflow boundary reduce the standard deviation of the velocity fluctuations by 20% near the flame anchoring point, thereby encouraging an attached flame for case two. Acoustic fluctuations appear to be an important source of these velocity fluctuations. To verify this we assume an upstream traveling pressure disturbance. In this case, the acoustic velocity fluctuations can be calculated using $u_{ac}(t) = -p'(t)/(\rho_0 c_0)$. Here, p' is the pressure fluctuation whereas ρ_0 and c_0 are the reference values for density and speed of sound. The acoustic velocity fluctuations u_{ac} are computed from the instantaneous pressure fluctuations p' in the x_1–x_2 plane at $x_3 = 0$ mm. At each instant the spatial average of u_{ac} over this plane is taken, and the resulting time series is plotted in Fig. 8b. The reference values ρ_0 and c_0 are obtained in the same plane by calculating the time averaged values of ρ and c. Comparing the data in Fig. 8b, it is found that the acoustic velocity fluctuations are in

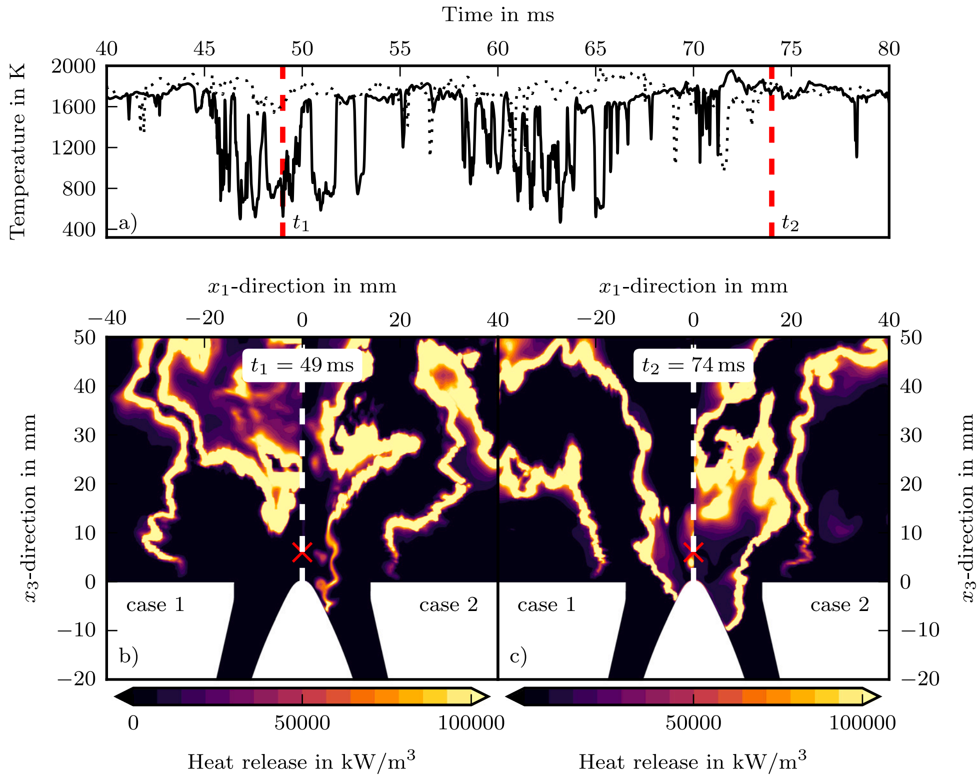

Fig. 7. Comparison of the temporal evolution of the temperature above the burner as well as instantaneous heat release for case 1 and case 2 at two different time instances. In (a) the temperature over time is extracted at the location marked in the contour plots. (——) case 1, (······) case 2. On the left half of the contour plots (b) and (c) case 1 is shown whereas on the right half case 2 is displayed.

phase with the velocity fluctuations displayed in Fig. 8a. Additionally, higher values are found for case one as compared to case two. This leads to the conclusion that the fluctuations at the flame anchoring point are indeed influenced by acoustic effects inside the combustion device. These findings align well with the observations of [40] where the authors investigate a different swirl burner with acoustic excitation. Depending on the excitation amplitudes, a lifted or attached flame is obtained. Additionally, a switching between attached and lifted flame is also reported for the swirl burner considered in the present study, though for different operating conditions (cf. [7,22]). Summarizing, at the considered operational point, case two yields results closer to experimental findings. This indicates that a correct amplitude of pressure oscillation is important for a realistic computation of this case. Moreover, frequent lift-off events that have been reported in previous numerical investigations (cf. [16,17]) are not observed for case two. According to the temperature data, these lift-off events are also absent in the experimental studies of [3].

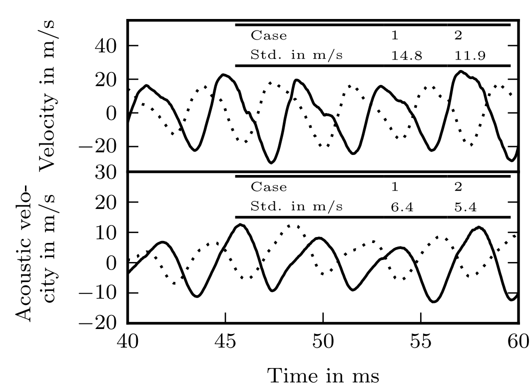

Fig. 8. (a) velocity fluctuations and (b) acoustic velocity fluctuations at the entrance into the combustion chamber in the x_1–x_2 plane at $x_3 = 0$ mm. (——) case 1, (······) case 2.

4.3. Uncertainties concerning the operational point

In [3] it is indicated that at a height of $x_3 = 80$ mm above the base plate the mixture should be homogeneous and in chemical equilibrium. The corresponding measured single shot data for temperature and mixture fraction are shown in Fig. 9a. Based on these data, standard deviations of 4.95% for temperature and 5.75% for mixture fraction are obtained (cf. Table 3). For both, temperature and mixture fraction these values exceed the measurement tolerances given in [3]. At the operating conditions considered here, this means that the combustion gases are not yet fully mixed, and are also not in chemical equilibrium either in some cases. This is evidenced by the presence of a few outliers with temperatures considerably lower than the equilibrium temperature. Further, considering the average of the mixture fraction indicated by the vertical line in Fig. 9a, a relative error of 5.88% to the nominal value of $z_{\text{nom.}} = 0.0391$ is found. In [3] it is suspected that a combination of errors from the flow-meters and Raman measurements could be responsible for these differences. This assumption appears, however, to be unlikely. For one, the results from the simulation of cases two and three given in Figs. 9b and 9c reveal that a similar spread is obtained as compared to the experimental results in Fig. 9a. Also the standard deviations (cf. Table 3) display a very close agreement to experiments for both cases. However, differences are found for the average mixture fractions indicated by the vertical lines in Fig. 9. Here, case three does show the best agreement with the measurement data. This reveals that for the measurements a systematic error in the operational point towards the fuel rich regime is present. The observed differences cannot be explained through a combination of errors between flow-meters and Raman measurement, but they can be

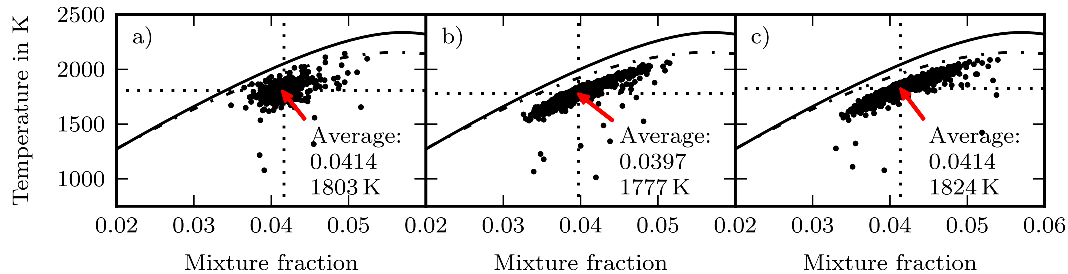

Fig. 9. Temperature over mixture fraction at $x_3 = 80\,\mathrm{mm}$. (a) measurements from [3], (b) case 2, (c) case 3. (——) adiabatic equilibrium, (–·–·) laminar flame with strain rate $a = 1\ \mathrm{s}^{-1}$.

Table 3
Standard deviations of mixture fraction and temperature corresponding to results shown in Fig. 9.

Variable	exp. [3]	case 2	case 3
Std. mixture frac.	5.75%	6.27%	6.49%
Std. temperature	4.95%	4.57%	4.83%

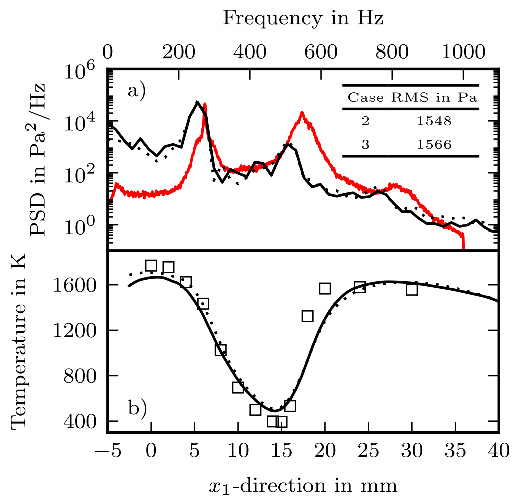

Fig. 10. Comparison of case 2 and case 3. (a) power spectral density of the pressure inside the combustion chamber. (b) temperature above the burner at $x_3 = 6\,\mathrm{mm}$. (——) case 2, (······) case 3, (——) measurements from [16], (□) measurements from [3].

attributed solely to a shift in the operational point that lies within the flow-meters accuracy. Comparing the results for cases two and three, a slight improvement in the agreement to the experimental data for the averaged temperatures close to the base plate is found. This is displayed in Fig. 10b and confirms the shift of the operational point present in the experimental data. However, considering Fig. 10a, the pressure signal does not seem to be as sensitive towards the operational point.

4.4. Validation of the computational model

So far, case three yields the best results in comparison to the experimental data presented. Hence, starting from this point, only case three is considered for the following discussions and investigations. However, first a rigorous validation is required for case three in order to draw further conclusions regarding the occurring phenomena inside the investigated swirl combustor. For this purpose, the additional measurement data available from [3] are used. This includes velocity data as well as data for density, temperature, and mass fractions for major species. Further, OH*-Chemiluminescence and planar laser-induced OH fluorescence measurement results are present. As an example, a comparison against the experimental data for the averaged axial velocities, the averaged fuel mass fractions and the respective standard deviations is given in Fig. 11. Here, an exceptional agreement with the measurement data is found. This very good agreement extends to the remaining available measurement data from [3]. For brevity, these data are not shown here. However, the complete dataset is provided in the supplemental material *MMC S1*. Also the proposed feedback loop of the self sustained pulsations as described in [3] is reproduced and confirmed. A more detailed description, together with a short video sequence, is provided in the supplementary material *MMC S1* and *Video S3*. To assure that the computed modes of the occurring pressure oscillations align with prior observations made for this combustion device, a multiresolution proper orthogonal decomposition (MRPOD) according to [8,41,42] is performed (this method is also used in [43] for the identification of thermoacoustic modes). A short description of the method alongside the chosen frequency intervals analyzed is given in Appendix A. The resulting first spatial MRPOD pressure modes in the frequency band $I_1 = [100, 390]\,\mathrm{Hz}$ and $I_2 = [390, 540]\,\mathrm{Hz}$ are displayed in Fig. 12. These two MRPOD modes are the dominant modes in their respective frequency bands and contain 88% and 87% of the relative energy. Alongside the contours in the x_1–x_3 plane, extracts following a path through the combustion device are displayed. It is revealed, that according to the first spatial mode in I_1 denoted by $\varphi_{1,I_1}(p)$, the air plenum and the combustion chamber oscillate in phase, whilst larger oscillations are found in the air plenum as compared to the combustion chamber. By contrast, the first spatial mode in I_2 however, shows that the chamber and air plenum oscillate in phase opposition. This is in line with the observations made by [37,38] where similar results concerning the mode shapes are found using a Helmholtz solver.

4.5. Technical premixing of fuel and air

To mix fuel and air, a jet-in-crossflow configuration is used in the present burner. Here, a fuel jet is injected into a crossflow of air inside each swirler vane. This is done through dedicated fuel ports. For this reason, a good mixing of fuel and air is typically assumed for the investigated burner, i.e. the gases entering the combustion chamber are considered to be reasonably well mixed [2,3,22,37,38,44–49]. However, as variations in the equivalence ratio are known to be an important driver of thermoacoustic instability, even small inhomogeneities might be significant for the present case. This is even more important as also experimental data of [3] confirms a certain amount of unmixedness directly above the central body. In order to obtain an estimate of the quality of mixing, two mixing efficiency factors

$$\eta_{\mathrm{mix},1} = \frac{\dot{m}_{\mathrm{mixed}}}{\dot{m}_{\mathrm{total}}} = \frac{\int_A \psi \rho u_i \,\mathrm{d}A}{\int_A \rho u_i \,\mathrm{d}A}, \tag{15}$$

$$\text{with} \quad \psi = \begin{cases} 1, & \text{if } (1-\epsilon) f_{\mathrm{nom.}} < f < (1+\epsilon) f_{\mathrm{nom.}} \\ 0, & \text{otherwise,} \end{cases}$$

and

$$\eta_{\mathrm{mix},2} = \frac{\sqrt{\frac{1}{A}\int_A f_{\sigma^2}\,\mathrm{d}A}}{\frac{1}{A}\int_A f\,\mathrm{d}A}, \tag{16}$$

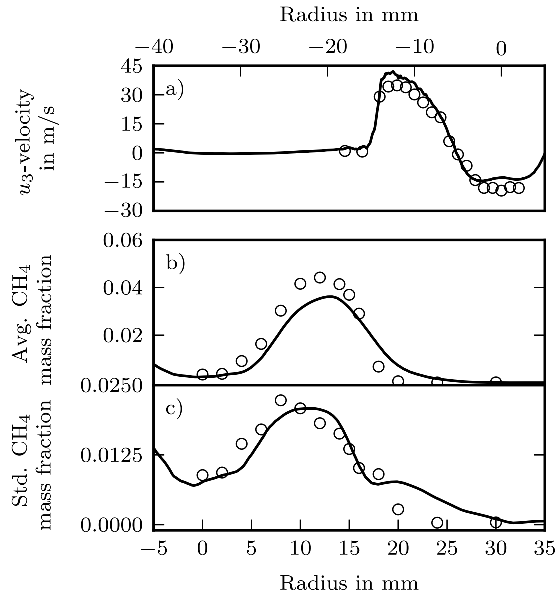

Fig. 11. Comparison with the measurement results from [3]. (a) averaged axial velocity at $x_3 = 1.5\,\mathrm{mm}$. (b) averaged fuel mass fraction at $x_3 = 6\,\mathrm{mm}$. (c) standard deviation of the fuel mass fraction at $x_3 = 6\,\mathrm{mm}$. (——) case 3, (○) measurements.

are introduced and evaluated at various locations in the swirler and duct sections. The first metric given by Eq. (15) loosely follows the approach of [50,51]. Here, the ratio of mixed and total area weighted averaged mass flows is calculated. For this purpose, the mixed mass flow is computed using a masking function based on the deviation of the averaged mixture fraction f from the nominal mixture fraction $f_{\mathrm{nom.}}$ by a threshold ϵ. While $\eta_{\mathrm{mix},1}$ gives an estimate concerning the homogeneity of local mixture fraction (high values indicate a good mixing), the variance of mixture fraction is equally important. In a well mixed setting this variance becomes small. Thus, the ratio of the area weighted averaged variance of the mixture fraction f_{σ^2} with the area weighted averaged mixture fraction is calculated as described in Eq. (16). Both metrics are evaluated on five slices as indicated on the right side of Fig. 13. The corresponding results for $\eta_{\mathrm{mix},1}$ and $\eta_{\mathrm{mix},2}$ are shown on the left side of Fig. 13. It is apparent that according to the evaluated metrics a rather poor mixing is obtained directly at the exit of the swirler at the cylindrical slice C1. Towards the exit of the duct the mixing is getting better as indicated by the increasing values for $\eta_{\mathrm{mix},1}$ and the decreasing values of $\eta_{\mathrm{mix},2}$. This shows that a large part of mixing is happening in the duct rather than inside the swirler vanes and therefore contradicts the general assumption of well mixedness due to the jet-in-crossflow configuration. To take a closer look into the swirler region where the fuel is injected into the air flow Fig. 14 is given. Here, Fig. 14a displays the phase averaged pressure in the air plenum and combustion chamber whereas the averaged velocities at the swirler entrance as well as the fuel injection ports are given in Fig. 14b. Additionally to the velocities, the phase averaged jet momentum ratio is plotted. Finally, in Figs. 14c–f a section of the swirler and duct is displayed where streamlines based on the phase averaged velocities as well as isocontours for the methane mass fractions are shown for the phases ϕ_3, ϕ_4, ϕ_6 and ϕ_1. Starting from the phase averaged pressure signals displayed in Fig. 14a it is apparent that the combustion chamber pressure exceeds the air plenum pressure in the phases ϕ_2 to ϕ_3. This leads to a modulated mass flow into the combustion chamber which is an essential part of the thermoacoustic oscillation cycle of the present swirl flame (cf. [3,17,21]). However, this reversal in pressure does not only impact the processes in the combustion chamber but influences also the flow inside the swirler vanes and consequently the mixing of fuel and air. Considering the phase averaged velocities of the jet and the crossflow in Fig. 14b this becomes clear. As pressure oscillates, both the velocity of the jet and the crossflow are modulated. However, while the fuel jet maintains a rather high momentum throughout the whole oscillation cycle the crossflow does not. During phases ϕ_3 to ϕ_4 the crossflow nearly ceases, whereas peak crossflow velocities are observed during phases ϕ_6 to ϕ_8. Computing the momentum ratio of crossflow and jet velocities a wide spread of values during an averaged oscillation cycle is revealed (cf. Fig. 14b). The momentum ratio peaks between phases ϕ_3 and ϕ_4 obtaining values of almost 900 while a very small momentum ratio is obtained at phase ϕ_6. For reference, the simple correlation $x_{3,\mathrm{pen.}} = 1.15 d_{\mathrm{jet}} J^{0.5}$ proposed in [52] yields a momentum ratio of $J = 22$ for a jet diameter of $d_{\mathrm{jet}} = 1\,\mathrm{mm}$, with a jet penetration depth of $x_{3,\mathrm{pen.}} = 5.375\,\mathrm{mm}$ into the center of the swirler vanes. Overall, this indicates that for the present thermoacoustically unstable operational point the jet-in-crossflow configuration does not operate as expected for large parts of the oscillation cycle. This becomes even more apparent considering Figs. 14c–f. At phase ϕ_3 displayed in Fig. 14c the crossflow velocity of air is low compared to the jet velocity of the fuel stream through the fuel ports. This results in a large momentum ratio and the fuel jets impinge onto the top walls of the swirler vanes where fuel accumulates close to the wall. Continuing with phase ϕ_4 in Fig. 14d, the crossflow accelerates and the momentum ratio decreases whilst still being too high to achieve a good mixing as fuel continues to impinge on the upper walls of the swirler vanes. For high crossflow velocities such as in phase ϕ_6 the conditions are reversed (cf. Fig. 14e). Here, the momentum ratio is too small in order to achieve good mixing and the fuel jet is not able to penetrate far into the crossflow. However, due to the high crossflow velocities the accumulated fuel rich regions close to the upper walls of the swirler vanes are being convected into the duct section. Finally, moving to the next phase in the cycle, the crossflow velocities decrease again and at least for phase ϕ_1 displayed in Fig. 14f a good mixing appears to take place inside the swirler vanes, temporarily. This is characterized by the fuel jet neither impinging the upper swirler vane walls nor being pushed towards the bottom walls. Overall this reveals that the conditions inside the swirler are more complex as often expected. This means that for an accurate numerical simulation a high amount of resolution is required to correctly represent the mixing of fuel and air at the operational point considered here.

4.6. *Flame type and coherent flow structures*

In general, the present model combustor is known to operate with two distinct flame types. One is a M-shaped flame and the other is a V-shaped flame. This notation stems from the characteristic shapes of the averaged OH*-Chemiluminescence measurements. Essentially, the M-shaped flame is associated with a flame that is lifted from the nozzle whereas the V-shaped flame remains attached. Whether the V- or M-shaped flame is present depends on the operational point and is, therefore, mainly a function of thermal power and equivalence ratio. A detailed experimental study for the perfectly premixed configuration is presented in [5], mapping a wide range of operational points. The authors show that only for M-shaped flames an unsteady coherent flow structure known as precessing vortex core (PVC) is able to emerge. Based on linear stability analysis, the authors identify density gradients as the cause of PVC-suppression for V-shaped flames. However, this hypothesis is recently challenged in [9] where a disruption of the internal flow feedback at the tip of the central body is proposed as the main cause for PVC-suppression. As such, the investigation of the PVC-suppression appears to be still an active field of research for this burner. In [5], operational points are found that display an unstable behavior, resulting in a constant switching between M- and V-shaped flames. Despite applying a perfectly premixed configuration, it is worth noting that the operational point investigated here is in the close vicinity of such an unstable flame. However, as shown in Section 4.2, the present

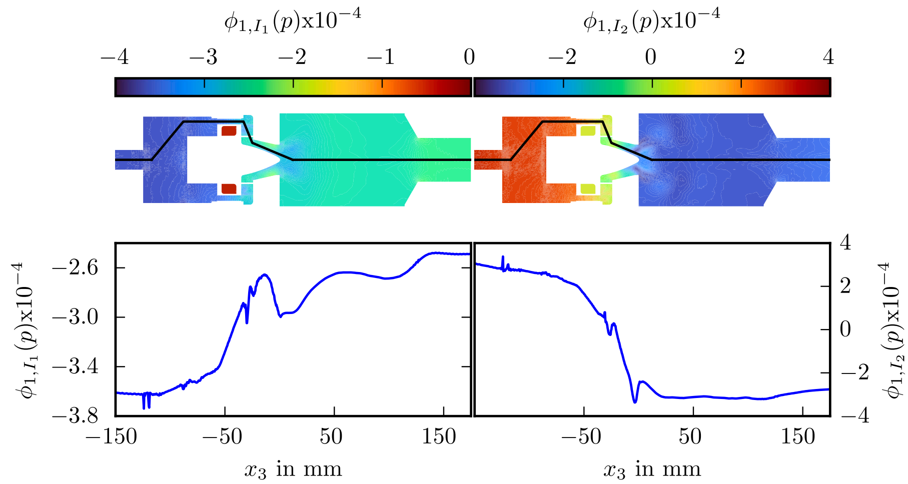

Fig. 12. Spatial MRPOD pressure modes $\varphi_{1,I_1}(p)$ (left) and $\varphi_{1,I_2}(p)$ (right) for interval I_1 and I_2 in the x_1–x_3 plane (top) and extracted along a path (bottom) for case 3. The path is displayed in the contour plots through (——).

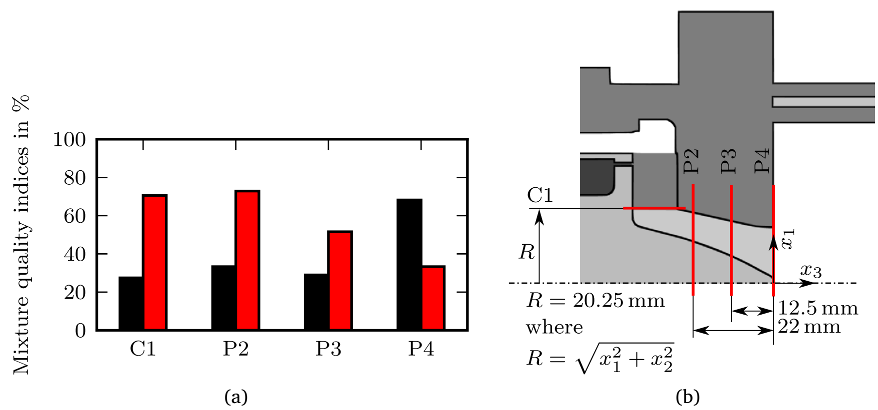

Fig. 13. Comparison of mixture indices as defined by Eq. (15) (■) for ϵ = 10% and Eq. (16) (■), evaluated at the cylindrical surface C1 and the planes P2, P3 and P4 indicated in the schematic drawing on the right side based on the averaged flow field data.

operational point measured by [3] is essentially an attached flame and hence a V-shaped flame. This is confirmed further by the OH*-Chemiluminescence measurements presented in [3] also given in the supplementary material *MMC S1*. Still, in the numerical data sporadic events of low temperature above the central body are present even for case three. Whether these events coincide with lift-off and shape switch of the flame as reported in [5] is investigated in the following. For this purpose, according to [5] the flow asymmetry in the x_1–x_3 plane is evaluated using

$$a(t) = \sum_{x_1,x_3} \left| \begin{pmatrix} u_a(x_1,x_3,t) \\ u_r(x_1,x_3,t) \\ u_\theta(x_1,x_3,t) \end{pmatrix} - \begin{pmatrix} u_a(-x_1,x_3,t) \\ u_r(-x_1,x_3,t) \\ u_\theta(-x_1,x_3,t) \end{pmatrix} \right|^2, \tag{17}$$

with u_a, u_r, and u_θ being the axial, radial, and tangential velocity components. The resulting flow asymmetry together with the temperature in a monitor point placed at $x_3 = 6$ mm is plotted over time in Fig. 15a. Alongside the flow asymmetry, velocity streamlines as well as the computed hydroxyl mass fraction in the x_1–x_3 plane at $x_2 = 0$ mm for two distinctive timesteps are given in Figs. 15b–c and Figs. 15d–e, respectively. Starting with the flow asymmetry over time given in Fig. 15a, the signal oscillates without major outliers up to about 77 ms. Between 77 ms to 86 ms a sudden peak in flow asymmetry is observed followed by a second peak. Another similar event is recorded between 93 ms to 102 ms. For the remaining signal no major outliers are found. Concerning the temperature above the central body, temporarily lower values are found together with these higher flow asymmetries. According to [5], an increase in flow asymmetry might indicate the presence of a PVC and likewise a switch in flame shape. Such a PVC can be recognized in the swirled flow field through a zig-zag flow pattern in the streamline plots in the respective plane. Now, as an example, results for two distinctive timesteps are picked from the time series as indicated by the dashed vertical lines in Fig. 15a. The first result is evaluated at about $t = 45$ ms having a low flow asymmetry whereas the second timestep at $t = 80$ ms resides within the first peak of flow asymmetry. Their corresponding velocity streamline plots are given in Figs. 15b–c. Comparing Fig. 15b and Fig. 15c differences are apparent. While for Fig. 15b a symmetry in the flow patterns with respect to the x_3-axis is visible, a characteristic zig-zag pattern emerges in Fig. 15c. This zig-zag pattern already suggests the presence of a PVC. Interestingly, by comparing the contour plots of the hydroxyl mass fraction at the same time instances in Fig. 15d-e identical patterns as described in [5] are found. In detail, at $t = 45$ ms an attached flame is found whereas for $t = 80$ ms a clear detachment of the flame from the central body is observed. In order to clarify if the observed zig-zag pattern in Fig. 15c stems from the presence of a PVC structure, the high-order filtered Q-criterion is analyzed. The high-order filtering of the Q-criterion is necessary because in the present refined simulation large coherent structures such as a PVC are fully masked by the small resolved vortices. For the high-order filtering, the implicit filter of [53] is applied following the approach of [54] for unstructured

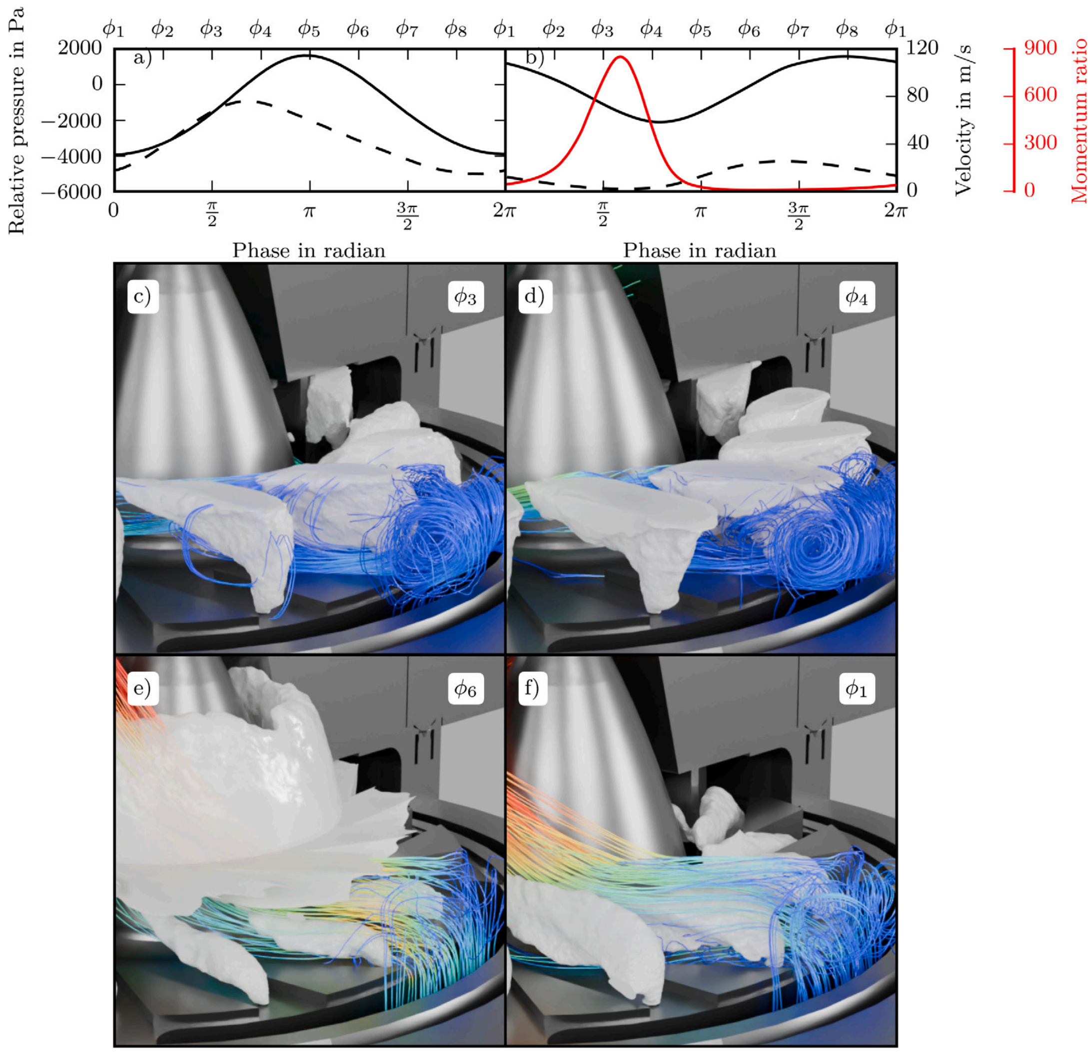

Fig. 14. Mixing of fuel and air inside the swirler vanes. (a) phase averaged pressure in the combustion chamber (- - -) and air plenum (——). (b) phase averaged velocity of the jet (——), crossflow (- - -), and jet momentum ratio (——). (c)–(f) cut through the swirler showing phases averaged velocity streamlines and methane mass fraction isovolumes ($Y_{CH_4} = 0.06$).

grids. The visualizations shown in Figs. 15f–g, are generated using an eighth order implicit filter with a width of 14 mm. Comparing Fig. 15f and Fig. 15g, the differences are obvious. For $t = 80$ ms a large helical structure representing the PVC is visible whereas for $t = 45$ ms no such clear structure emerges. To further clarify whether a PVC is present, a modal analysis of the pressure is performed using the MRPOD-method. According to [5] the PVC at the given operational point and under perfectly premixed conditions emerges at a frequency of 595 Hz. Hence, the frequency band for the MRPOD is set to $I_3 = [540, 3250]$ Hz (cf. Fig. 17). Inspecting the resulting spatial pressure modes from the modal analysis, two modes (φ_{5,I_3} and φ_{6,I_3}) associated with a PVC structure are found. The corresponding contours shown in Figs. 16a and 16b reveal the expected zig-zag patterns. Moreover, the associated three-dimensional isocontours shown in Fig. 16c clearly reveal the helical nature of the emerging structure. A time-frequency analysis of the temporal coefficients a_{5,I_3} and a_{6,I_3} given in Figs. 16d and 16e shows that this PVC structure does not only occur sporadically but almost periodically over the time of the simulation. However, these scaleograms also show that the PVC is most pronounced at $t = 80$ ms where it is also observed via the filtered Q-criterion. Furthermore, the PVC does not appear to prevail at a fixed frequency but exists over a frequency range as can also be observed by the broad spectra given in Figs. 16f and 16g where the PSDs of the temporal coefficients a_{5,I_3} and a_{6,I_3} are shown. This is due to the strong thermoacoustic instabilities occurring in the technically premixed case which strongly modulate the volumetric flow rate as shown in Fig. 16f leading to this transient behavior. Additionally, at $t = 45$ ms faint traces of the PVC are also detected in the modal analysis where it is not found in the instantaneous flow fields. Also, as indicated in Fig. 15d, the flame remains attached. This shows that in the present LES most of the time a V-shaped flame without a pronounced PVC is obtained. Still, sporadic events exist for which the flame detaches and switches to a M-shaped flame as indicated in [5]. Together with the M-shaped flame a strong PVC is able to emerge for a short period of time. However, shortly after the switch to a M-shaped flame the flame reattaches and switches back to a V-shape resulting in the very good agreement with the experimental data of [3].

5. Summary and conclusions

Based on the given results, it is shown that the self-excited thermoacoustic operational point chosen in [3] resides close to a point where the flame becomes unstable switching from an attached V-shape to an detached M-shape. This type of behavior is already observed in literature for perfect premixing of fuel and air in [5,7,8]. However, for perfectly premixed operation, the duration of these transitions

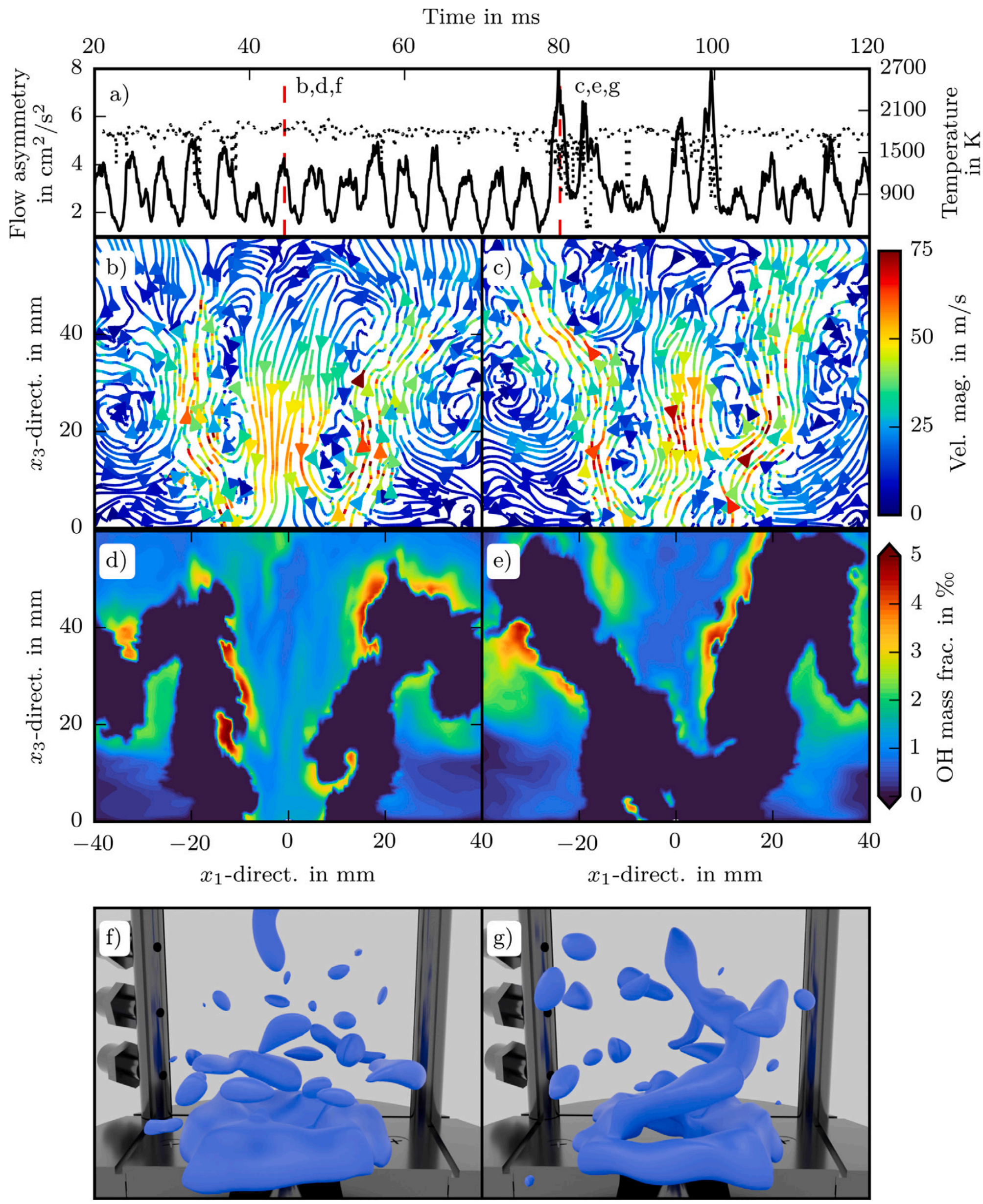

Fig. 15. Flame shapes and coherent flow structures. (a) flow asymmetry (——), temperature above central body (······) and selected timesteps (- - -). (b, c) velocity streamlines in x_1–x_3 plane. (d, e) hydroxyl mass fraction in x_1–x_3 plane. (f, g) isosurfaces of high-order filtered Q-criterion ($Q_{\mathrm{qcrit}} = 10^7\ \mathrm{s}^{-2}$).

spans over several milliseconds in contrast to the present work. The transitions reported here (under technical premixing) occur within the duration of a single acoustic oscillation (i.e., a few milliseconds) which is in line with the experimental observations of [22] for technical premixing at very similar operating conditions in terms of thermal power and equivalence ratio. Likewise, intermittent changes between lifted and attached flames within a few milliseconds are also reported in [11] for technically premixed operation with methane (equivalence ratio and thermal power are 0.65 and 20 kW, respectively, in [11]). In [11], the occurrence of a PVC is also reported during phases of flame lift-off. Hence, the experimental data [11,22] appear to support the present numerical findings. Furthermore, this conclusion is supported by the strong influence of the amplitude of pressure oscillations onto the flame's shape and location as demonstrated by a comparison of cases one and two. By reducing the reflection coefficient at the outflow boundary for case two, the amplitude of pressure oscillation inside the combustion chamber is lowered. While the exact mechanisms that leads to flame lift-off cannot fully be isolated in this complex flow, these lower acoustic velocities likely decrease both strain rates and convective transport, thereby promoting an attached flame. Therefore, the low temperature events above the central body are reduced which leads to an excellent agreement in temperature close to the central body with respect to the measurement data. This influence of the amplitude of pressure oscillation on the flame shape has so far been neglected in previous work on this operational point. In this work we showed that for the considered operational point this has a major influence on the overall results. Nonetheless, intermittent events of low temperature above the central body are still present as shown for case three. These low temperature events coincide with a switch of flame shape as described in [5] albeit for perfect premixed conditions. Alongside the temporary switch from V-shaped flame towards an M-shaped flame a strong PVC is able to emerge for a short period of time. Due to the thermoacoustic instabilities and the resulting strong modulation of the volume flow rate at the nozzle exit, the PVC occurs

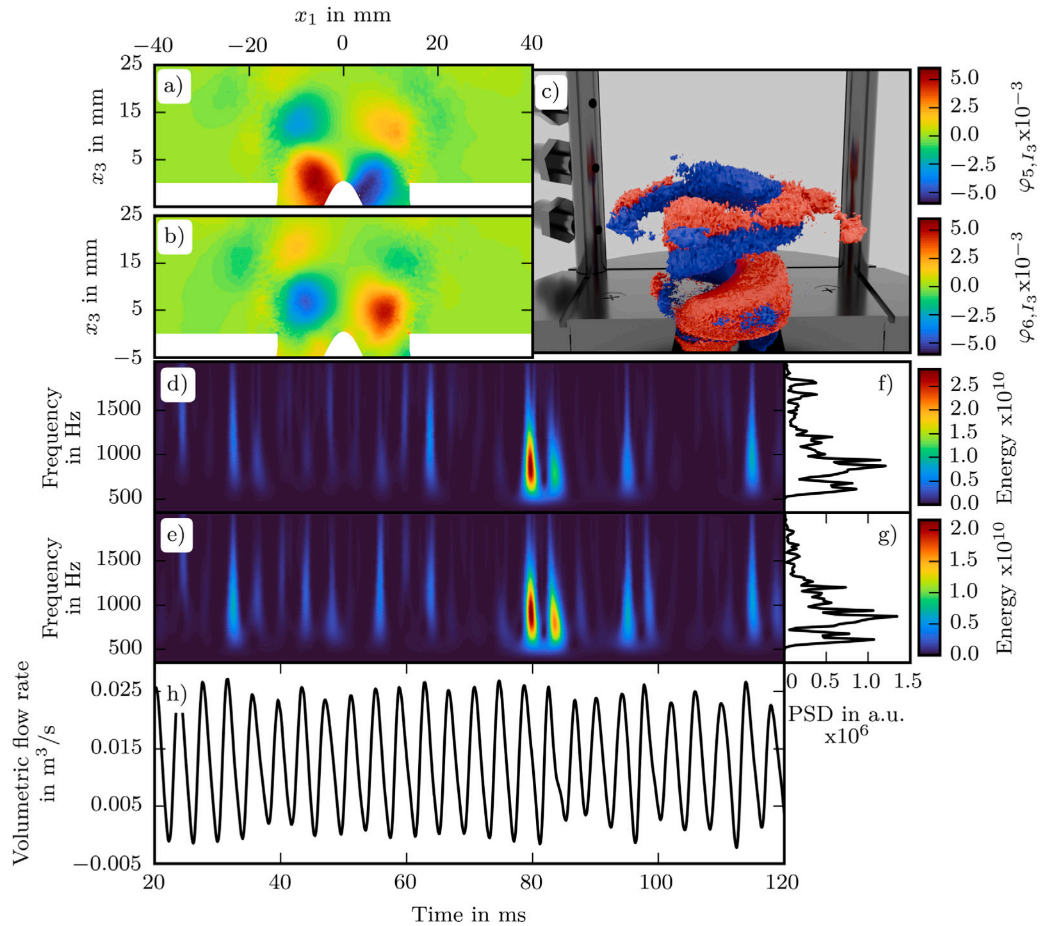

Fig. 16. Modal analysis for frequency band I_3. (a) slice in the x_1–x_3 plane of the spatial mode φ_{5,I_3}. (b) slice in the x_1–x_3 plane of the spatial mode φ_{6,I_3}. (c) isocontours showing the helical structures of φ_{5,I_3} (red) and φ_{6,I_3} (blue). (d) and (e) showing the scaleograms of the temporal coefficients a_{5,I_3} and a_{6,I_3}. (f) and (g) PSD of the temporal coefficients a_{5,I_3} and a_{6,I_3}. (h) volumetric flow rate at the nozzle exit.

over a frequency range instead of a fixed frequency as often observed in literature for other operating conditions. In contrast to numerical investigations found in literature, flame lift off only happens sporadically and on average an attached flame similar to the experiments of [3] is found. Further, it is numerically shown that during the measurements of [3] a slight shift towards a richer regime occurred. Although these errors are within the tolerances of the mass-flow controllers, taking them into account does slightly improve the overall agreement with the experimental data for case three in contrast to case two. Furthermore, the processes within the swirler as well as the mixing of fuel and air are more complex as typically assumed, necessitating careful modeling to ensure accurate results. Consequently, a superior agreement between numerical computation and experimental measurements is achieved for the considered operational point.

CRediT authorship contribution statement

Michael Pries: Conceptualization, Data curation, Formal analysis, Investigation, Methodology, Software, Validation, Visualization, Writing – original draft. **Andreas Fiolitakis:** Conceptualization, Methodology, Software, Supervision, Writing – review & editing.

Declaration of competing interest

The authors declare that they have no known competing financial interests or personal relationships that could have appeared to influence the work reported in this paper.

Acknowledgments

The authors gratefully acknowledge the late Prof. Dr. Peter Gerlinger for his invaluable contributions to the presented studies and investigations. His insightful discussions and mentorship were essential to the success of this work. We also are grateful for the scientific support and HPC resources provided by the German Aerospace Center (DLR). The HPC system CARA is partially funded by “Saxon State Ministry for Economic Affairs, Labour and Transport” and “Federal Ministry for Economic Affairs and Climate Action, Germany”. The HPC system CARO is partially funded by “Ministry of Science and Culture of Lower Saxony, Germany” and “Federal Ministry for Economic Affairs and Climate Action, Germany”.

Appendix A. Multiresolution proper orthogonal decomposition

The multiresolution proper orthogonal decomposition (MRPOD) offers the possibility to perform proper orthogonal decompositions on discrete frequency bands. To conduct such a multiresolution analysis a maximum-overlap discrete packet wavelet transform is employed. In this work, this is based on Daubechies least asymmetric, compactly supported wavelet with a filter length of 16 and a decomposition level of 7. The applied frequency bands are denoted by I and given in Fig. 17 alongside the PSD for case three. In this sense, the MRPOD of a fluctuating quantity $\zeta(x_i,t)'$ in the frequency band I_1 is expressed as

$$\zeta(x_i,t)' = \sum_{k=1}^{N} a_{k,I_1}(\zeta,t)\varphi_{k,I_1}(\zeta,x_i). \tag{18}$$

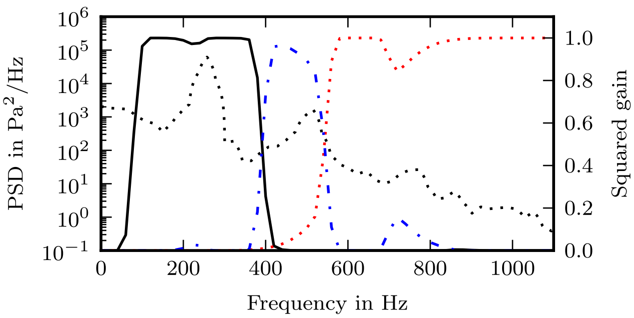

Fig. 17. Definition of frequency bands used for the MRPOD analysis. Squared gain of the intervals I_1 (——), I_2 (-·-·-), and I_3 (······). Power spectral density of pressure for case 3 (······).

Here, $a_{k,I_1}(\zeta,t)$ represents the kth temporal coefficient of the frequency band I_1, $\varphi_{k,I_1}(\zeta,x_i)$ the corresponding spatial mode, and N the length of the time series. Further, $\zeta(x_i,t)'$ denotes the fluctuating part of the decomposition expressed by $\zeta(x_i,t) = \langle\zeta(x_i,t)\rangle + \zeta(x_i,t)'$, where $\langle\zeta(x_i,t)\rangle$ represents the time average of the quantity $\zeta(x_i,t)$. A more detailed explanation of the method can be found in [8].

Appendix B. Supplementary data

Supplementary material related to this article can be found online at https://doi.org/10.1016/j.jaecs.2026.100524.

References

[1] Weigand P, Duan XR, Meier W, Meier U, Aigner M, Bérat C. Experimental investigations of an oscillating lean premixed CH_4/air swirl flame in a gas turbine model combustor. In: Proceedings of the European combustion meeting 2005. 2005.

[2] Weigand P, Meier W, Duan X, Aigner M. Laser-based investigations of thermoacoustic instabilities in a lean premixed gas turbine model combustor. J Eng Gas Turb Power 2006;129(3):664–71. http://dx.doi.org/10.1115/1.2718224.

[3] Meier W, Weigand P, Duan XR, Giezendanner-Thoben R. Detailed characterization of the dynamics of thermoacoustic pulsation in a lean premixed swirl flame. Combust Flame 2007;150(1):2–26. http://dx.doi.org/10.1016/j.combustflame.2007.04.002.

[4] Steinberg A, Arndt C, Meier W. Parametric study of vortex structures and their dynamics in swirl-stabilized combustion. Proc Combust Inst 2013;34(2):3117–25. http://dx.doi.org/10.1016/j.proci.2012.05.015.

[5] Oberleithner K, Stöhr M, Im SH, Arndt CM, Steinberg AM. Formation and flame-induced suppression of the precessing vortex core in a swirl combustor: Experiments and linear stability analysis. Combust Flame 2015;162(8):3100–14. http://dx.doi.org/10.1016/j.combustflame.2015.02.015.

[6] Yin Z, Nau P, Meier W. Responses of combustor surface temperature to flame shape transitions in a turbulent bi-stable swirl flame. Exp Therm Fluid Sci 2017;82:50–7. http://dx.doi.org/10.1016/j.expthermflusci.2016.11.004.

[7] Stöhr M, Oberleithner K, Sieber M, Yin Z, Meier W. Experimental study of transient mechanisms of bistable flame shape transitions in a swirl combustor. J Eng Gas Turb Power 2017;140(1):011503. http://dx.doi.org/10.1115/1.4037724.

[8] Yin Z, Stöhr M. Time–frequency localisation of intermittent dynamics in a bistable turbulent swirl flame. J Fluid Mech 2020;882:A30. http://dx.doi.org/10.1017/jfm.2019.762.

[9] Gupta S, Datta A, Hemchandra S, Boxx I. Precessing vortex core suppression in a swirl stabilized combustor with hydrogen addition. In: Proceedings of the ASME turbo expo 2023: turbomachinery technical conference and exposition. Turbo expo, Volume 3A: Combustion, Fuels, and Emissions, 2023, http://dx.doi.org/10.1115/GT2023-100617, V03AT04A002.

[10] Kushwaha A, Kasthuri P, Pawar S, Sujith RI, Chterev I, Boxx I. Dynamical characterization of thermoacoustic oscillations in a hydrogen-enriched partially premixed swirl-stabilized methane/air combustor. J Eng Gas Turb Power 2021;143(12):121022. http://dx.doi.org/10.1115/1.4052091.

[11] Datta A, Gupta S, Chterev I, Boxx I, Hemchandra S. Impact of hydrogen addition on the thermoacoustic instability and precessing vortex core dynamics in a CH_4/H_2/air technically premixed combustor. J Eng Gas Turb Power 2021;144(2):021013. http://dx.doi.org/10.1115/1.4052202.

[12] Franzelli B, Riber E, Gicquel LYM, Poinsot T. Large Eddy Simulation of combustion instabilities in a lean partially premixed swirled flame. Combust Flame 2012;159(2):621–37. http://dx.doi.org/10.1016/j.combustflame.2011.08.004.

[13] Lourier J-M, Noll B, Aigner M. Extension of a compressible pressure-based solver for reacting flows. In: 19th AIAA/CEAS aeroacoustics conference. 2013, http://dx.doi.org/10.2514/6.2013-2101, No.: AIAA-2013-2101.

[14] Lourier J-M, Noll B, Aigner M. Large Eddy Simulation of a thermoacoustic instability within a swirl-stabilzed burner using impedance boundary conditions. In: Proceedings of ASME turbo expo 2014: turbine technical conference and exposition. 2014, http://dx.doi.org/10.1115/GT2014-26200, No.: GT2014-26200.

[15] Lourier J-M, Eberle C, Noll B, Aigner M. Influence of turbulence-chemistry interaction modeling on the structure and the stability of a swirl-stabilized flame. In: Proceedings of ASME turbo expo 2015: turbine technical conference and exposition. 2015, http://dx.doi.org/10.1115/GT2015-43174, No.: GT2015-43174.

[16] Lourier J-M, Stöhr M, Noll B, Werner S, Fiolitakis A. Scale adaptive simulation of a thermoacoustic instability in a partially premixed lean swirl combustor. Combust Flame 2017;183:343–57. http://dx.doi.org/10.1016/j.combustflame.2017.02.024.

[17] Fredrich D, Jones WP, Marquis AJ. A combined oscillation cycle involving self-excited thermo-acoustic and hydrodynamic instability mechanisms. Phys Fluids 2021;33(8):085122. http://dx.doi.org/10.1063/5.0057521.

[18] Fredrich D, Jones WP, Marquis AJ. Thermo-acoustic instabilities in the PRECCINSTA combustor investigated using a compressible LES-PDF approach. Flow Turbul Combust 2021;106:1399–415. http://dx.doi.org/10.1007/s10494-020-00177-3.

[19] Zhao S, Bhairapurada K, Tayyab M, Mercier R, Boivin P. Lattice-Boltzmann modeling of the quiet and unstable PRECCINSTA burner modes. Comput & Fluids 2023;260:105898. http://dx.doi.org/10.1016/j.compfluid.2023.105898.

[20] Gövert S, Lipkowicz JT, Janus B. Compressible Large Eddy Simulations of thermoacoustic instabilities in the PRECCINSTA combustor using flamelet generated manifolds with dynamic thickened flame model. In: Proceedings of the ASME turbo expo 2023. 2023, http://dx.doi.org/10.1115/1.4063419, No.: GT2023-103438.

[21] Pries M, Fiolitakis A, Hadef R, Gerlinger P. Numerical and experimental investigation of self excited thermoacoustic instabilities in a lean, partially premixed swirl flame. In: AIAA SCITECH 2024 forum. 2024, http://dx.doi.org/10.2514/6.2024-0592, No.: AIAA-2024-0592.

[22] Arndt C, Steinberg AM, Boxx IG, Meier W, Aigner M, Carter CD. Flow-field and flame dynamics of a gas turbine model combustor during transition between thermo-acoustically stable and unstable states. In: Proceedings of the ASME turbo expo 2010: power of land, sea and air. Turbo expo, Volume 2: Combustion, Fuels and Emissions, Parts A and B, 2010, p. 677–87. http://dx.doi.org/10.1115/GT2010-22830.

[23] Roux S, Lartigue G, Poinsot T, Meier U, Bérat C. Studies of mean and unsteady flow in a swirled combustor using experiments, acoustic analysis, and Large Eddy Simulations. Combust Flame 2005;141(1):40–54. http://dx.doi.org/10.1016/j.combustflame.2004.12.007.

[24] Pries M, Fiolitakis A, Gerlinger P. An implicit splitting scheme with characteristic boundary conditions for compressible reactive flows on unstructured grids. J Comput Appl Math 2024;437:115446. http://dx.doi.org/10.1016/j.cam.2023.115446.

[25] Setzwein F, Ess P, Gerlinger P. An implicit high-order k-exact finite-volume approach on vertex-centered unstructured grids for incompressible flows. J Comput Phys 2021;446:110629. http://dx.doi.org/10.1016/j.jcp.2021.110629.

[26] Fiolitakis A, Pries M. A novel approach to the characteristic splitting scheme for mildly compressible flows based on the weighted averaged flux method. J Comput Phys 2024;513:113197. http://dx.doi.org/10.1016/j.jcp.2024.113197.

[27] Barth T, Jespersen D. The design and application of upwind schemes on unstructured meshes. In: 27th aerospace sciences meeting. 1989, http://dx.doi.org/10.2514/6.1989-366.

[28] Erlebacher G, Hussaini MY, Speziale CG, Zang TA. Toward the Large-Eddy Simulation of compressible turbulent flows. J Fluid Mech 1992;238:155–85. http://dx.doi.org/10.1017/S0022112092001678.

[29] Nicoud F, Ducros F. Subgrid-scale stress modelling based on the square of the velocity gradient tensor. Flow Turbul Combust 1999;62:183–200. http://dx.doi.org/10.1023/A:1009995426001.

[30] Kathrotia T, Oßwald P, Naumann C, Richter S, Köhler M. Combustion kinetics of alternative jet fuels, part-II: Reaction model for fuel surrogate. Fuel 2021;302:120736. http://dx.doi.org/10.1016/j.fuel.2021.120736.

[31] Gerlinger P. Investigation of an assumed PDF approach for finite-rate chemistry. Combust Sci Technol 2003;175:841–72. http://dx.doi.org/10.1080/00102200302410.

[32] Fredrich D. A numerical method for the prediction of combustion instabilities [Ph.D. thesis], Imperial College London, Mechanical Engineering; 2019, http://dx.doi.org/10.25560/95144.

[33] Poinsot T, Lele S. Boundary conditions for direct simulations of compressible viscous flows. J Comput Phys 1992;101(1):104–29. http://dx.doi.org/10.1016/0021-9991(92)90046-2.

[34] Pries M, Fiolitakis A, Gerlinger P. Impact of combustion and outflow modeling on self-excited thermoacoustic instabilities in a lean premixed swirl-flame. In: AIAA SCITECH 2025 forum. 2025, http://dx.doi.org/10.2514/6.2025-2087, No.: AIAA-2025-2087.

[35] Rudy DH, Strikwerda JC. A nonreflecting outflow boundary condition for subsonic Navier-Stokes calculations. J Comput Phys 1980;36(1):55–70. http://dx.doi.org/10.1016/0021-9991(80)90174-6.

[36] Arndt CM, Nau P, Meier W. Characterization of wall temperature distributions in a gas turbine model combustor measured by 2D phosphor thermometry. Proc Combust Inst 2021;38(1):1867–75. http://dx.doi.org/10.1016/j.proci.2020.06.088.

[37] Agostinelli PW, Laera D, Boxx I, Gicquel L, Poinsot T. Impact of wall heat transfer in Large Eddy Simulation of flame dynamics in a swirled combustion chamber. Combust Flame 2021;234:111728. http://dx.doi.org/10.1016/j.combustflame.2021.111728.

[38] Agostinelli PW, Laera D, Chterev I, Boxx I, Gicquel L, Poinsot T. On the impact of H_2-enrichment on flame structure and combustion dynamics of a lean partially-premixed turbulent swirling flame. Combust Flame 2022;241:112120. http://dx.doi.org/10.1016/j.combustflame.2022.112120.

[39] Fredrich D, Jones WP, Marquis AJ. The stochastic fields method applied to a partially premixed swirl flame with wall heat transfer. Combust Flame 2019;205:446–56. http://dx.doi.org/10.1016/j.combustflame.2019.04.012.

[40] Bellows BD, Bobba MK, Forte A, Seitzman JM, Lieuwen T. Flame transfer function saturation mechanisms in a swirl-stabilized combustor. Proc Combust Inst 2007;31(2):3181–8. http://dx.doi.org/10.1016/j.proci.2006.07.138.

[41] Grader M, Yin Z, Geigle KP, Gerlinger P. Influence of flow field dynamics on soot evolution in an aero-engine model combustor. Proc Combust Inst 2021;38(4):6421–9. http://dx.doi.org/10.1016/j.proci.2020.05.019.

[42] Grader M, Gerlinger P. Influence of operating conditions on flow field dynamics and soot formation in an aero-engine model combustor. Combust Flame 2023;258:112712. http://dx.doi.org/10.1016/j.combustflame.2023.112712, Special issue and Perspective on the Chemistry and Physics of Carbonaceious Particle Formation.

[43] Fiolitakis A, Pries M, Lammel O, Kathrotia T. Numerical and experimental investigation of high-frequency thermoacoustic instabilities in a jet-stabilized burner. J Propuls Power 2026;42:267–84. http://dx.doi.org/10.2514/1.B39885.

[44] Meier W, Boxx I, Stöhr M, Carter CD. Laser-based investigations in gas turbine model combustors. Exp Fluids 2010;49:865–82. http://dx.doi.org/10.1007/s00348-010-0889-x.

[45] Arndt C, Steinberg AM, Boxx IG, Meier W, Aigner M. Influence of heat release on swirl flow dynamics from high speed laser measurements in a gas turbine model combustor. In: Conference: 23rd international colloquium on the dynamics of explosions and reactive systems. 2011.

[46] Ansari N, Strakey PA, Goldin GM, Givi P. Filtered density function simulation of a realistic swirled combustor. Proc Combust Inst 2015;35(2):1433–42. http://dx.doi.org/10.1016/j.proci.2014.05.042.

[47] Fredrich D, Galot-Lavallée S. Large Eddy Simulation of a gas turbine model combustor using the Eulerian subgrid probability density function method. In: Digital proceedings of the 8th European combustion meeting. 2017, p. 1803–8.

[48] Fredrich D, Jones WP, Marquis AJ. Application of the Eulerian subgrid probability density function method in the Large Eddy Simulation of a partially premixed swirl flame. Combust Sci Technol 2019;191(1):137–50. http://dx.doi.org/10.1080/00102202.2018.1452396.

[49] Agostinelli PW, Rochette B, Laera D, adn B. Cuenot JD, Gicquel L. Static mesh adaptation for reliable Large Eddy Simulation of turbulent reacting flows. Phys Fluids 2021;33:035141. http://dx.doi.org/10.1063/5.0040719.

[50] Mao M, Riggins DW, McClinton CR. Numerical simulation of transverse fuel injection. 1991, Document ID: 19910011784.

[51] Roos T, Pudsey A, Bricalli M, Ogawa H. Numerical investigation of upstream cavity enhanced fuel mixing in scramjet combustors. Acta Astronaut 2020;169:50–65. http://dx.doi.org/10.1016/j.actaastro.2019.12.033.

[52] Lefebvre AH, Ballal DR. Gas turbine combustion: alternative fuels and emissions. third ed. CRC Press; 2010, http://dx.doi.org/10.1201/9781420086058.

[53] Raymond WH, Garder A. A review of recursive and implicit filters. Mon Weather Rev 1991;119(2):477–95. http://dx.doi.org/10.1175/1520-0493(1991)119<0477:ARORAI>2.0.CO;2.

[54] Guedot L, Lartigue G, Moureau V. Design of implicit high-order filters on unstructured grids for the identification of large-scale features in Large-Eddy Simulation and application to a swirl burner. Phys Fluids 2015;27(4):045107. http://dx.doi.org/10.1063/1.4917280.